Entropy generation in the woven mesh regenerator filler of cryocoolers

IOP Conf. Series: Materials Science and Engineering **755** (2020) 012064 doi:10.1088/1757-899X/755/1/012064

Entropy generation in the woven mesh regenerator filler of cryocoolers

Ali Ghavami, Tao Fang and S Mostafa Ghiaasiaan
Georgia Institute of Technology, G.W. Woodruff School of Mechanical Engineering, Atlanta, GA, USA 30332

ali.ghavami@gatech.edu

Abstract. The regenerator is a key component of a pulse tube cryocooler, and is also a major contributor to irreversibility and losses in the cryocooler. In this study a method for the assessment of losses in cryocooler regenerators based on entropy generation is proposed. Pore-level CFD simulations are performed for woven mesh regenerator filler by defining periodically repeating unit cells. Simulations are performed for steady-state (uni-directional) as well as periodic flows. It is shown that entropy generation in periodic flow is higher than in steady flow, and is sensitive to operating parameters as well as small geometric irregularities. It is proposed that by optimization of the microstructure of regenerator fillers the entropy generation and losses can be minimized.

1. Introduction

Regenerators are one of the key components in regenerative cryocoolers including GM, pulse tube and Stirling cryocoolers. To improve the performance of regeneration, this component should have high heat capacity, low axial thermal conduction, low friction and high porosity. Regenerator fillers come in various geometries, including powders composed of spheres, metal foams, wire mesh, and more recently carefully designed micro-manufactured structures. To comprehensively optimize thermal efficiency of a regenerator filler, both first and second laws of thermodynamic must be considered. The first law analysis aims to maximize the Nusselt number, while the second law analysis is meant to minimize the entropy generation by minimizing the exergy destruction and losses. Bejan [1, 2] provides a good discussion about entropy generation minimization in various thermal and flow systems including porous media. The combined first and second law analysis may particularly be useful for modern micro manufactured fillers where the pore level geometric details can be controlled in order to minimize losses. This study is part of a project that is meant to develop a CFD-assisted methodology to optimize regenerator fillers based on pore-level first and second-law analysis.

Woven mesh regenerator fillers are analysed in this paper. These fillers, also known as wire packing, are among the most popular choices because of their low cost, easy manufacturability, and high thermal efficiency. Woven mesh regenerators have been the subject of many investigations in the past. Roberts et al. [3] and Nam et al. [4] investigated the regenerator friction factor and ineffectiveness for 400 mesh stainless steel and 200 mesh stainless steel fillers, respectively. Hsu et al. [5] studied steady state and low frequency periodic flow in woven mesh regenerator. These experiments were performed on regenerators with pore characteristic lengths larger than a millimetre, however. Pore-level experiments when pore characteristic size is of the order of 10 microns is very difficult even with miniaturized instruments because of their flow disturbances. As a result, numerical tools and computational fluid

dynamics (CFD) are often used for elucidation of pore-level flow behaviour. For example, Chen et al. [6] recently investigated convective heat transfer in woven mesh regenerators during oscillating flow.

In this paper, entropy generation is investigated by performing three-dimensional pore level CFD simulations of flow phenomena in a woven mesh regenerator, for steady state as well as oscillating flow. This geometry is depicted in Figure 1 which has been borrowed from [6]. For steady flow, the effects of geometric size, wire diameter, porosity, geometry irregularity and operating conditions are evaluated to optimize the regenerator and minimize exergy destruction. For oscillating flow, entropy generation is investigated for one geometry and for different Reynolds numbers.

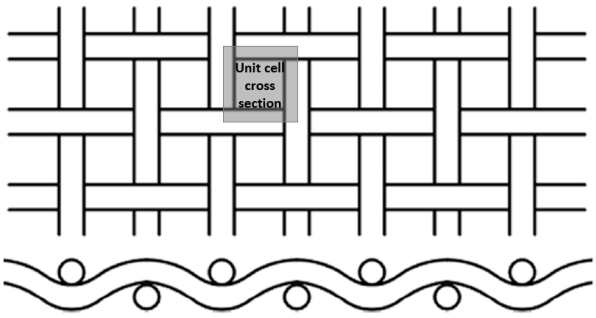

Figure 1. Woven mesh regenerator structure [6].

2. Geometric configuration of computational domain

Regenerators often have a complex geometry. The idea of unit cell is therefore often used to reduce the computational time. A unit cell is the minimum segment of a geometry in the flow field which represents a periodically repeating pattern for the entire complex geometry. The cross section of unit cell is shown in Figure 1. The unit cell approach has successfully been used for analyzing different regenerators in previous works [7, 8].

Figure 2 (a) and (b) show the solid and fluid parts, respectively, of the unit cell in a woven regenerator for steady state analysis. The inlet and outlet surfaces should match exactly for performing cyclic boundary conditions in the flow direction. The solid surface boundaries parallel to the flow direction are considered as a wall and the remaining fluid interface parallel to the main flow is modeled as a symmetry boundary condition. Figure 2 (c) represents the computational domain for oscillating flow. For oscillating flow, Pathak et al. [9] showed that the entrance effects disappear only after the first few unit cells when buffer zones are placed at the two ends of a row of unit cells, and fully developed flow is achieved in the remainder of the unit cells. Therefore, five unit cells along with buffer zones each with the lengths of $5D_h$, where D_h is hydraulic diameter (characteristic length), are used as presentative of a regenerator. The simulation results for the third (middle) unit cell are then assumed to represent the behavior of all unit cells in a prototypical regenerator.

Figure 2 (a) also depicts parameters D, the wire diameter, H, parallel distance between wires, and V, height of mesh filler. These parameters are varied for the optimization of the woven mesh regenerator. Porosity, Φ, is calculated by dividing fluid volume by the total volume of unit cell. Hydraulic diameter, $D_h$is calculated by,

$$D_h = \frac{4V_f}{A_f} \tag{1}$$

where V_f is fluid volume in a unit cell and A_f represents total wetted surface area in a unit cell.

Table 1 summarizes the geometric parameters for all unit cell cases studied here. Case 1 is chosen as the reference test case. For investigating the effect of geometry irregularities, it is assumed that a particle partially blocked one of the unit cells in the domain. In Cases 8 and 9 spherical particles with diameters of 10 μm and 20 μm, respectively, are placed at the center of unit cell number 1.

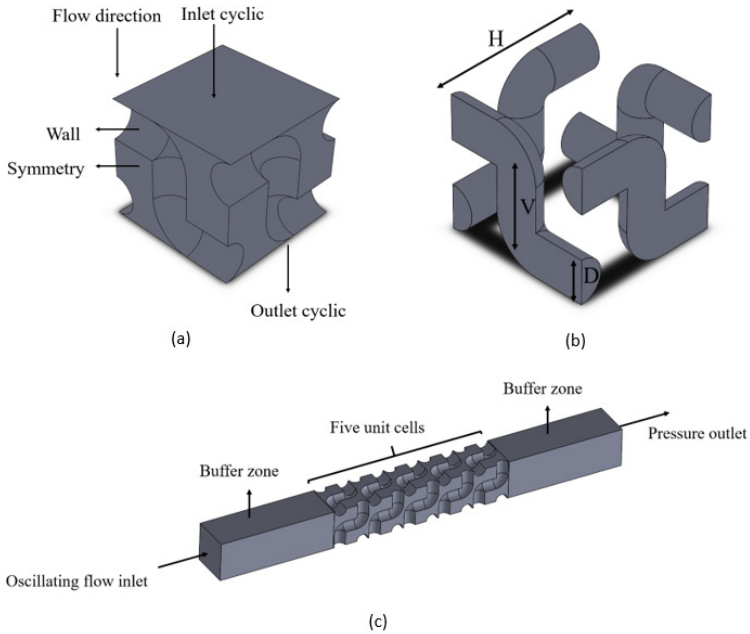

Figure 2. Computational domain (a) solid part of unit cell for steady state condition, (b) fluid part of unit cell for steady state, (c) fluid part of domain for oscillating flow calculation.

Table 1. Unit cell geometry configurations for steady state analysis.

Case number	D (μm)	H (μm)	V (μm)	Porosity, Φ	D_h (μm)
1	30	100	60	0.76	110
2	20	100	60	0.88	153
3	40	100	60	0.64	71
4	30	70	60	0.62	50
5	30	130	60	0.83	156
6	30	100	40	0.74	87
7	30	100	80	0.78	109
8	Geometry irregularity, case 1 partially blocked by particle with diameter 10 μm				
9	Geometry irregularity, case 1 partially blocked by particle with diameter 20 μm				

3. Theory and method of solution

The continuity, momentum and energy equations which are solved in three-dimensions for pore level scale analysis, and the solid-phase energy conservation equation are:

$$\frac{\partial u_j}{\partial x_j} = 0 \tag{2}$$

$$\frac{\partial u_i}{\partial t} + \frac{\partial}{\partial x_j} u_j u_i = -\frac{1}{\rho_f}\frac{\partial P}{\partial x_i} + \frac{\partial}{\partial x_j}\nu_f\left(\frac{\partial u_i}{\partial x_j} + \frac{\partial u_j}{\partial x_i}\right) \tag{3}$$

$$\rho_f c_f\left(\frac{\partial T}{\partial t} + \frac{\partial}{\partial x_j} u_j T\right) = \frac{\partial}{\partial x_j}\left(k_f \frac{\partial T}{\partial x_j}\right) \tag{4}$$

$$\rho_s c_s\left(\frac{\partial T}{\partial t}\right) = \frac{\partial}{\partial x_j}\left(k_s \frac{\partial T}{\partial x_j}\right) \tag{5}$$

where ν_f, ρ_f, k_f and c_f are kinematic viscosity, density, thermal conductivity, and specific heat of the fluid, respectively. Furthermore, ρ_s, c_s, and k_s are, respectively, the density, specific heat and thermal conductivity of the solid phase. Equation (5) is only solved for oscillating flow cases, where we deal with a conjugate heat transfer process. Since unit cell approach is chosen, volume averaged parameters

over a single unit cell will be presented and discussed here. Volume average value of a fluid-related variable is defined as:

$$\langle \beta \rangle = \frac{1}{V_f} \int_{V_f} \beta dV \tag{6}$$

For oscillating flow, in addition to volume averaging, cycle averaging is also used, whereby:

$$\langle \beta \rangle_{cycle} = \frac{1}{t_{cycle}} \int_{t_{cycle}} \langle \beta \rangle \, dt \tag{7}$$

where $t_{cycle}$is the time period of one cycle in oscillating flow.

The total local volumetric entropy generation rate in the fluid, $\dot{S}_{gen}$, is caused by viscous dissipation, $\dot{S}_{g,FF}$, and heat transfer, $\dot{S}_{g,HT}$, where [10]:

$$\dot{S}_{gen} = \dot{S}_{g,FF} + \dot{S}_{g,HT} \tag{8}$$

$$\dot{S}_{g,FF} = \frac{\mu_f}{T} \left(\frac{\partial u_i}{\partial x_j} + \frac{\partial u_j}{\partial x_i} \right) \frac{\partial u_i}{\partial x_j} \tag{9}$$

$$\dot{S}_{g,HT} = \frac{k_f}{T^2} \left[\left(\frac{\partial T}{\partial x} \right)^2 + \left(\frac{\partial T}{\partial y} \right)^2 + \left(\frac{\partial T}{\partial z} \right)^2 \right] \tag{10}$$

where μ_f is the fluid dynamic viscosity and T is local temperature. The local entropy generation rate is normalized as shown in equation 11 [11] to define the non-dimensional local entropy generation rate , S_n. Once volume averaging is performed, the dimensionless volume average entropy generation, S_t, is accordingly derived.

$$S_n = \dot{S}_{gen} \frac{D_h^2}{k_f}, \qquad S_{n,FF} = \dot{S}_{g,FF} \frac{D_h^2}{k_f}, \quad S_{n,HT} = \dot{S}_{g,HT} \frac{D_h^2}{k_f},$$
$$S_t = \langle S_n \rangle = \frac{1}{V_f} \int_{V_f} S_n dV, \quad S_{t,FF} = \langle S_{n,FF} \rangle, \quad S_{t,HT} = \langle S_{n,HT} \rangle \tag{11}$$

Other dimensionless parameters that are used in the forthcoming discussions are the Reynolds number, the Nusselt number, and Bejan number, defined respectively as:

$$Re = \frac{\rho_f |\langle \vec{u} \rangle| D_h}{\mu_f}, Nu = \frac{\frac{q''}{\overline{T}_{wall} - \langle T_f \rangle} D_h}{k_f}, Be = \langle \frac{\dot{S}_{g,HT}}{\dot{S}_{g,FF} + \dot{S}_{g,HT}} \rangle \tag{12}$$

where Re is defined based on absolute volume-average velocity in steady state condition, and absolute cycle and volume-average value of velocity in oscillating flow. In calculating Nu, q'' represents the constant heat flux from all walls, $\overline{T}_{wall}$ is average temperature of all heated walls, and $\langle T_f \rangle$ is volume average temperature of fluid in a unit cell. Bejan number compares the contributions of heat transfer and viscous dissipation to irreversibility. The performance evaluation criterion (PEC) is the parameter which is used for optimization [11]:

$$PEC = \frac{Nu}{S_t} \tag{13}$$

4. Model setup and assumptions

ANSYS Fluent [12] is used for solving equations 2-5 for both steady state and oscillating flow cases. In steady state cases, a constant q'' is applied on all walls. This value changes from 250 W/m^2 to 1000 W/m^2. Laminar flow with low Re numbers is the range of interest, and Re number varies from 2 to 40. The working fluid is Helium at 3.87 MPa and in view of the small temperature variations in each unit cell, properties of Helium are assumed to be constant and correspond to 300 K.

In oscillating flow cases, an oscillating mass flow rate is applied at the inlet by a user defined function (UDF), according to:

$$\dot{m} = \dot{m}_{peak} sin(2\pi f t) \quad (14)$$

where f is the frequency of oscillating flow, and is set to 20Hz in this study. The outlet boundary is set equal to the regenerator working pressure. The temperature difference between the buffer zones in oscillating flow cases should be comparable to the steady state condition. For this reason, the average fluid temperature at the inlet and outlet of one unit cell is calculated in steady state flow and then the temperature difference is multiplied by five and is applied in oscillating flow.

The solid wire geometry is added to fluid computational domain for oscillating flow cases where conjugate heat transfer occurs. Solid wires are made of stainless steel with constant properties at 300 K. All fluid and solid boundaries parallel to the flow direction are set to symmetry boundary conditions in both buffer zones and the five unit cell zones.

Grid independency was analyzed by using maximum element sizes of $9 \times 10^{-6}m$, $5 \times 10^{-6}m$, $1 \times 10^{-6}m$, and $7 \times 10^{-7}m$ and grid-independent solution with less than 1% change in total entropy generation was achieved with $1 \times 10^{-6}m$ maximum element size. Eight inflation layers are also added at walls to capture the boundary layer effects.

Pressure based solver with SIMPLE scheme is used for both steady state and oscillating flow simulations. For the convergence criteria, the residual is set to 10^{-5} for continuity and momentum equations and 10^{-9} for energy equation. For oscillating flow the time step is set equal to 0.000156 s and fully converged results were achieved after 10 cycles.

5. Results and discussion

5.1. Steady flow

Figure 3 shows contour plots of temperature, velocity, and local total entropy generation at the steady state condition in case 1 at $Re = 18$ and $q" = 750\ W/m^2$. The complex geometry of the unit cell and heat transfer both lead to entropy generation. Both the velocity gradient and temperature gradient are higher at the heated wall boundaries which cause much higher irreversibility near the walls.

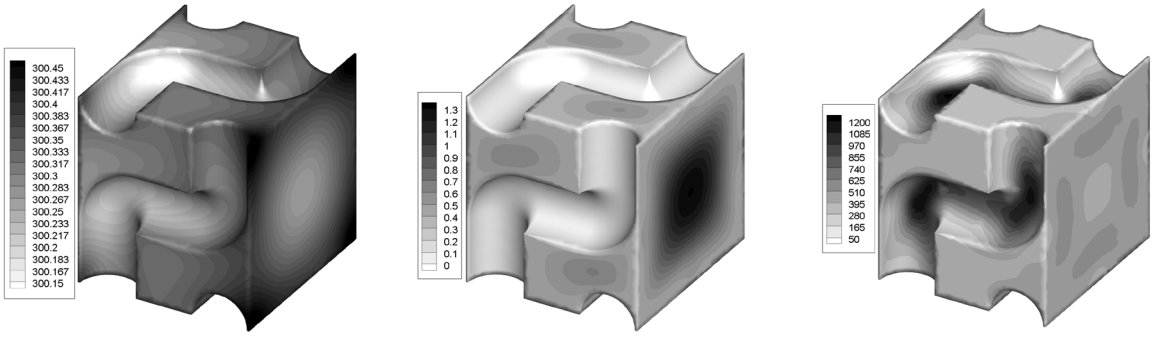

(a) (b) (c)

Figure 3. Contour plots of case number 1 at $Re = 18$ and $q" = 750\ W/m^2$, (a) temperature (K), (b) velocity magnitude (m/s), (c) local total volumetric entropy generation rate (W/m^3).

Figure 4 (a) compares the contributions of the viscous dissipation and heat transfer to entropy generation for case 1 with $q" = 750\ W/m^2$. As expected, increasing Re leads to increasing of the viscous dissipation portion. The monotonic reduction of heat transfer entropy generation is a result of assumed constant wall heat flux which leads to lower temperature gradients as Re is increased. The presence of a minimum point in the total entropy generation is evident, which occurs when entropy generation terms by viscous dissipation and heat transfer are equal. Figure 4 (b) shows the variation of Nusselt number at different Re for case 1. The Nusselt number is a weak function of Re since the flow is thermally developed laminar with low Re.

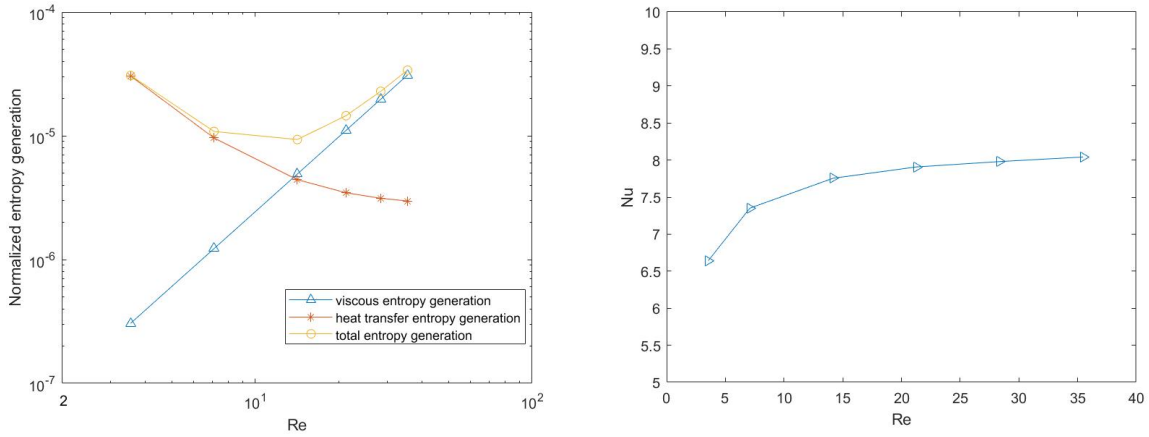

(a) (b)

Figure 4. Case 1 results, (a) normalized viscous, heat transfer and total volume average entropy generation rate with $q" = 750\ W/m^2$, (b) Nusselt number variation.

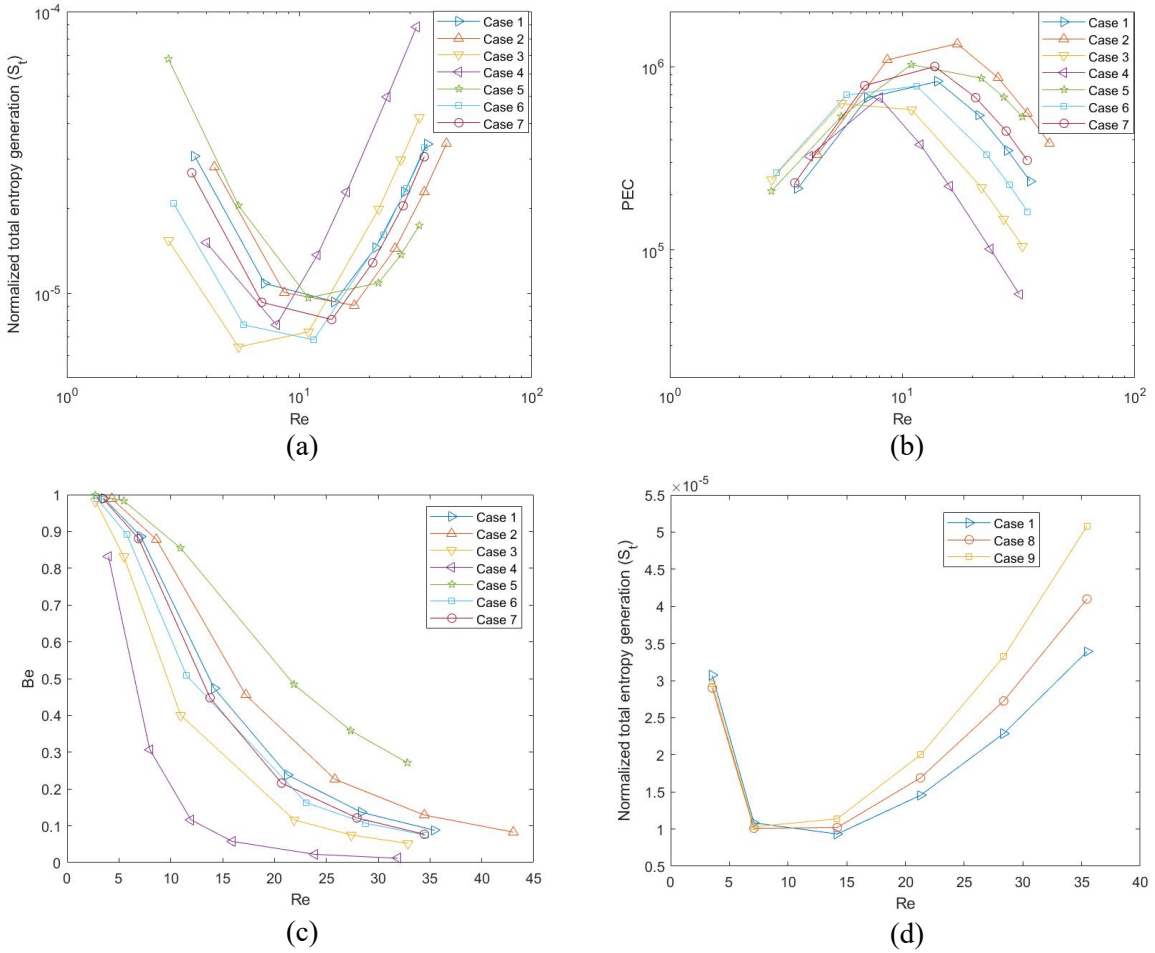

(a) (b)

(c) (d)

Figure 5. Comparison of all 9 steady flow cases at $q" = 750\ W/m^2$, (a) normalized total volumetric entropy generation, (b) performance evaluation criterion (*PEC*), (c) Bejan number, (d) effect of irregularity (unit cell partially blocked) on total entropy generation.

Figure 5 illustrates the effect of unit cell geometry on irreversibility, as well as the variation of *PEC* and Be with Re. As noted in Figure 5 (a) for every unit cell there is a Re value that leads to minima entropy generation, beyond which the total entropy generation increases because of enhanced viscous dissipation. This behavior results in the occurrence of maxima points in *PEC* variations as shown in Figure 5 (b). Comparing the unit cells 1 to 7, Figure 5 (b) indicates that cases with lower wire diameter (comparing cases 1,2, and 3), higher parallel distance between wires (comparing cases 1,4, and 5), and higher height (comparing cases 1,6, and 7) have better *PEC* at *Re* numbers beyond the maxima point. An opposite trend can be observed at *Re* numbers below the maxima point, however, where heat transfer plays a more important role. Figure 5 (c) shows Be decreases monotonically with increasing Re.

Figure 5 (d) shows the effect of geometric irregularities on entropy generation. It is assumed that the unit cell is partially blocked by a spherical particle. The presence of the particle at the middle of the unit cell increases the viscous dissipation and thereby causes higher entropy generation and as the diameter of the particle increases, the viscous entropy generation is increased. However, the heat transfer entropy, which is mainly generated around the heated walls, would not be affected by this blockage which leads to no change in heat entropy generation, and therefore no change in total entropy generation at very low Re where heat entropy generation is dominant.

Figure 6 shows the effect of wall heat flux in case 1. As expected higher heat flux causes higher total entropy generation and higher *Be* number. As shown in Figure 6 (a), the effect of heat flux is higher at lower *Re* where the contribution of heat transfer to the total entropy generation is higher.

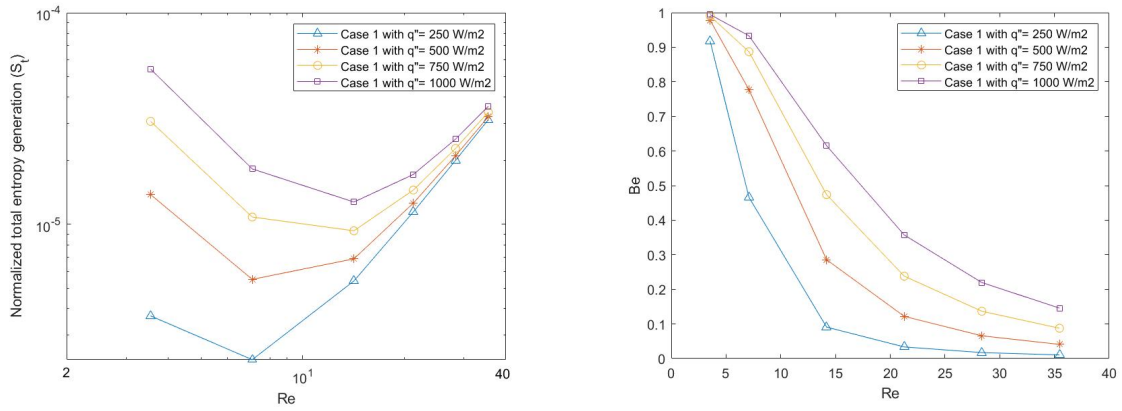

(a) (b)

Figure 6. The effect of wall heat flux on entropy generation of case 1.

5.2. Oscillating flow

Figure 7 shows the contours of local total entropy generation rate, temperature, and velocity magnitude at 1/8 and 1/4 cycle for case 1 at $Re = 34$. The inlet and outlet buffer zones are not shown. As shown in Figure 7 (d), the velocity inside the porous channel becomes essentially independent of the inlet in the second unit cell. Therefore, the volume average total entropy generation of the middle unit cell (the third unit cell) will be reported and discussed below.

Figure 8 compares the normalized volume average total entropy generation for steady state and oscillating flow condition at $f = 20Hz$ in case 1. Recall that for oscillating flow the entropy generation rate is cycle-averaged. It is noted that the total entropy generation is consistently higher in oscillating flow. This behavior happens mainly because of small vortices formation near the corners of flow passage due to the change in flow direction in oscillating flow, which leads to higher viscous dissipation. Simulations are underway for the elucidation of parametric dependencies in oscillating flow conditions.

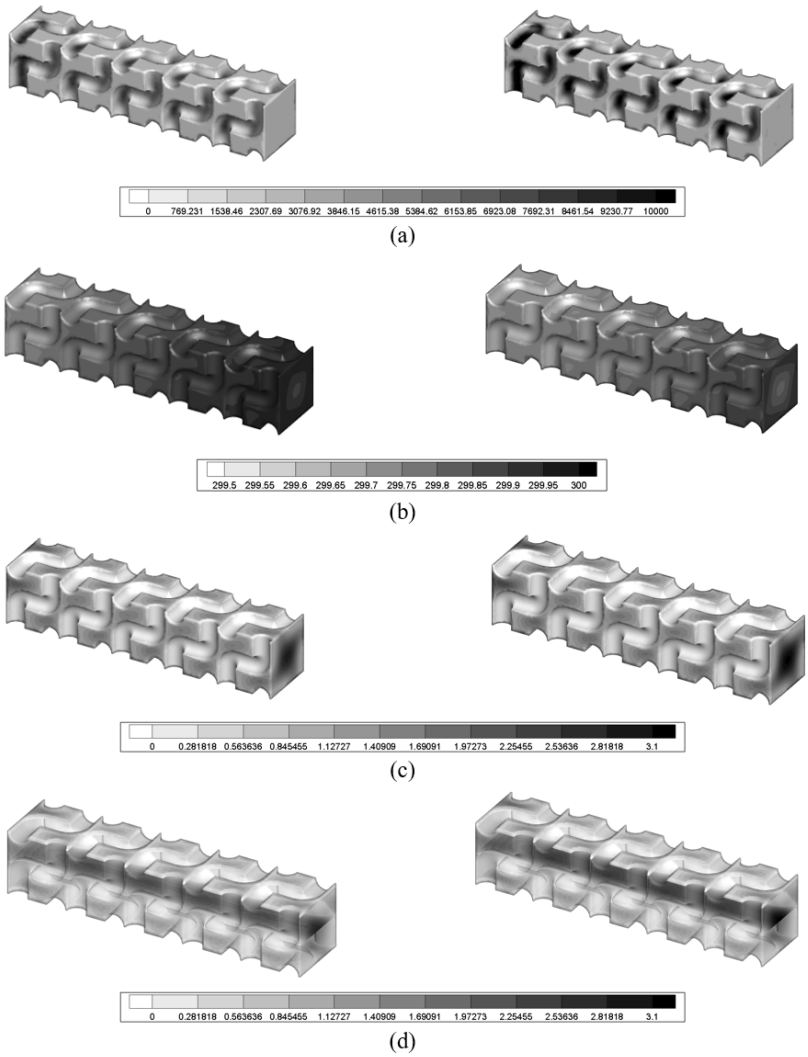

Figure 7. Contours of oscillating flow simulation at 1/8 cycle (left contours) and 1/4 cycle (right contours) for case 1 at $Re = 34$, (a) total entropy generation (W/m^3K), (b) temperature (K), (c) velocity magnitude (m/s), (d) velocity magnitude (m/s) at the middle and near symmetry surfaces.

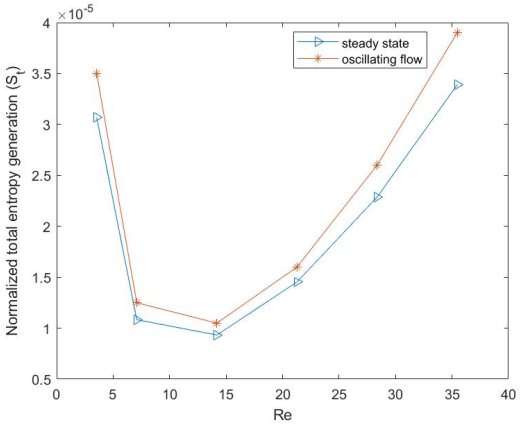

Figure 8. Normalized total entropy generation for steady state with $q" = 750\ W/m^2$ and oscillating flow for case 1 at $f = 20Hz$.

6. Conclusion

A pore-level CFD-assisted investigation was performed aimed at the elucidation of entropy generation in woven mesh regenerator fillers. Simulations were performed for both steady state and oscillating flow conditions and the results were compared. The simulations show that the optimum operating conditions are determined by the relative magnitudes of viscous dissipation and entropy generation due to heat transfer. For steady flow simulations where wall heat flux is assumed to be constant the contribution of viscos irreversibility increases with Re, while the contribution of heat transfer irreversibility monotonically diminishes. As a result, the optimum working conditions occur when the two contribution terms become equal. The effects of geometry irregularities and wall heat flux were also studied. Partial blockage of flow passages caused by particles can significantly increase entropy generation.

7. References

[1] Bejan, A. and Kestin, J., 1983. Entropy generation through heat and fluid flow. *Journal of Applied Mechanics*, **50**, p.475.

[2] Bejan, A., 1996. Entropy generation minimization: The new thermodynamics of finite-size devices and finite-time processes. *Journal of Applied Physics*, **79**(3), pp.1191-1218.

[3] Roberts, T.P. and Desai, P.V., 2004, June. Working fluid state properties measurements in medium and high frequency cryocoolers. In *AIP Conference Proceedings* (Vol. **710**, No. 1, pp. 1146-1153). AIP.

[4] Nam, K. and Jeong, S., 2002, May. Experimental study on the regenerator under actual operating conditions. In *AIP Conference Proceedings* (Vol. **613**, No. 1, pp. 977-984). AIP.

[5] Hsu, C.T., Fu, H. and Cheng, P., 1999. On pressure-velocity correlation of steady and oscillating flows in regenerators made of wire screens. *Journal of fluids engineering*, **121**(1), pp.52-56.

[6] Chen, S., Huang, Q., Liang, M., Chen, H., Chen, L. and Hou, Y., 2018. Numerical study on the heat transfer characteristics of oscillating flow in cryogenic regenerators. *Cryogenics*, **96**, pp.99-107.

[7] Ghavami, A., Kirkconnell, C., Ghiaasiaan, S.M., Chen, W. and Zagarola, M., 2018. Analysis of a Novel Micro-Structured Regenerator Filler.

[8] Pathak, M.G., Mulcahey, T.I. and Ghiaasiaan, S.M., 2013. Conjugate heat transfer during oscillatory laminar flow in porous media. *International Journal of Heat and Mass Transfer*, **66**, pp.23-30.

[9] Pathak, M.G. and Ghiaasiaan, S.M., 2011. Convective heat transfer and thermal dispersion during laminar pulsating flow in porous media. *International Journal of Thermal Sciences*, **50**(4), pp.440-448.

[10] Ebrahimi, A., Rikhtegar, F., Sabaghan, A. and Roohi, E., 2016. Heat transfer and entropy generation in a microchannel with longitudinal vortex generators using nanofluids. *Energy*, **101**, pp.190-201.

[11] Torabi, M., Torabi, M., Ghiaasiaan, S.M. and Peterson, G.P., 2017. The effect of Al2O3-water nanofluid on the heat transfer and entropy generation of laminar forced convection through isotropic porous media. *International Journal of Heat and Mass Transfer*, **111**, pp.804-816.

[12] Fluent, A., 2011. 14.5 User's Guide. *Fluent Inc., Lebanon, NH*.